

Interband electronic transitions and phase diagram of $\text{PbZr}_{1-x}\text{Ti}_x\text{O}_3$ ($0.05 \leq x \leq 0.70$)
ceramics: ellipsometric experiment and first-principles theory

This content has been downloaded from IOPscience. Please scroll down to see the full text.

2016 J. Phys. D: Appl. Phys. 49 275305

(<http://iopscience.iop.org/0022-3727/49/27/275305>)

View [the table of contents for this issue](#), or go to the [journal homepage](#) for more

Download details:

IP Address: 222.66.117.10

This content was downloaded on 27/06/2016 at 09:30

Please note that [terms and conditions apply](#).

Interband electronic transitions and phase diagram of $\text{PbZr}_{1-x}\text{Ti}_x\text{O}_3$ ($0.05 \leq x \leq 0.70$) ceramics: ellipsometric experiment and first-principles theory

M J Li¹, L P Xu¹, K Shi¹, J Z Zhang¹, X F Chen², Z G Hu¹, X L Dong²
and J H Chu¹

¹ Department of Electronic Engineering, East China Normal University, Shanghai 200241, People's Republic of China

² Key Laboratory of Inorganic Functional Materials and Devices, Shanghai Institute of Ceramics, Chinese Academy of Sciences, Shanghai 200050, People's Republic of China

E-mail: zghu@ee.ecnu.edu.cn

Received 26 September 2015, revised 1 May 2016

Accepted for publication 10 May 2016

Published 7 June 2016



Abstract

The thermal evolutions of optical properties and phase transitions of $\text{PbZr}_{1-x}\text{Ti}_x\text{O}_3$ (PZT) ceramics as the functions of Ti compositions have been systemically explored by means of temperature dependent ellipsometric spectra and first-principles calculations. Two interband electronic transitions have been obtained by fitting the second derivatives of the complex dielectric functions and the physical origins can be explained with the aid of theoretical calculations. Based on the interband transitions, the phase diagram of PZT ceramics can be well-established. Importantly, dramatic Zr-rich ion clusters at 70 K and two intermediate regions are captured. The Zr-side intermediate phase is attributed to the tilting competitions of high $[\text{FE}_{\text{R}(\text{HT})}]$ and low $[\text{FE}_{\text{R}(\text{LT})}]$ temperature rhombohedral structures. Moreover, a wider range of the monoclinic (M) region from $x = 0.28$ to 0.50 has been determined than previously reported. Interestingly, one can conclude that a more superior performance of PZT may be obtained with the larger M domains relying on external strains or fields.

Keywords: electronic transitions, spectroscopic ellipsometry, first-principles calculations, phase diagram

(Some figures may appear in colour only in the online journal)

1. Introduction

Ferroelectric and piezoelectric materials enjoy a wide range of applications in nonvolatile random access memories, actuators, optical-electric modulators, sensors, and electromechanical systems [1–4]. Among those materials, lead zirconate titanate $\text{PbZr}_{1-x}\text{Ti}_x\text{O}_3$ (PZT), as one of the most significant members, has been the focus due to superior ferroelectric and

piezoelectric properties. This material undergoes phase transitions from the Zr-rich to Ti-rich region while passing through an approximately vertical boundary named the ‘morphotropic phase boundary’ (MPB) at around $x = 0.48$ [5–7]. At the MPB range, the piezoelectric and dielectric properties of PZT reach a maximum since the higher activities of the peculiar structure consisting of various twin walls and intricate domain boundaries [8–10]. Since 1971, a systematic phase diagram of PZT has made a remarkable breakthrough for the understanding of structures and performance of PZT-based materials [11]. As we know, ferroelectric tetragonal phase (T) with the polar axis along pseudocubic [0 0 1] axes (hereinafter, the subscript p)



Original content from this work may be used under the terms of the [Creative Commons Attribution 3.0 licence](https://creativecommons.org/licenses/by/3.0/). Any further distribution of this work must maintain attribution to the author(s) and the title of the work, journal citation and DOI.

locates at the Ti-rich side. At the Zr-rich side, however, there is not merely a simple ferroelectric rhombohedral phase (R) with the polar axis along $[1\ 1\ 1]_p$ axes. Recently, considerable efforts have been made to investigate the complicated microstructures and phase transitions of PZT, especially the intermediate structures, for satisfying the ever-increasing (growth rate of 13% per year) market demands of piezoelectric actuators and realizing more extensive applications [12–15].

Fortunately, Noheda *et al* have first revealed that an intermediate monoclinic region with the polarization vector rotated towards $\langle 1\ 1\ 1 \rangle$ near the MPB separates T and R phases [16, 17]. As a subgroup of $P4mm$, $R3c$ and $R3m$, the M phase has suffered some passionate debates about whether it can be divided into a space group of Cm and another low symmetry Cc or whether there is a definite border among R, M, and T regions due to the disorder of the Pb atoms [18, 19]. On the other hand, it contains more than one intermediate phase in the PZT phase diagram. Near the PbZrO_3 (PZ) side, an antiferroelectric orthogonal (AFE_O) phase emerges with $Pbam$ space group, where the octahedron rotates around the $[1\ 1\ 0]_p$ axis. As the Ti concentration increases, the phase transformation is frustrated by the AFE_O displacement of the Pb^{2+} perpendicularly to the average FE direction $(1\ 1\ 1)$ [20]. An antiparallel arrangement of the cations along $[1\ 1\ 0]_p/[1\ 1\ 0]_p$ directions occurs at the boundary between the antiferroelectric (AFE) and ferroelectric (FE) phases. Based on similar work in La-doped PZT, another intermediate monoclinic region which allows continuous coupling of the tilt axis and polarization vector was proffered [21, 22]. Furthermore, a possible border of the intermediate region was determined around $x = 0.17$, which is regarded as the onset of the tilt instability in the R phase derived from the lattice disorder by spectroscopy measurements [15]. Although an abundance of PZT phase diagrams have been figured out to date, the issues about precise intermediate regions and whether two intermediate phases share the same inherent mechanism still remain. In addition, phase transformations of ferroelectric materials are associated with the mechanisms of electronic transitions. Therefore, it is extremely necessary for us to systematically investigate the phase diagram of PZT ceramics through non-destructive temperature dependent spectroscopy methods.

Recently, many spectral measurements, such as Raman scattering, infrared reflection, and spectroscopic ellipsometry, have reached successful results in optical properties, intrinsic electronic transitions and phase transformations [23–25]. Among various optical techniques, based on the variation of amplitude and phase of the incident polarized light after reflection from the samples, spectroscopic ellipsometry (SE) provides an effective method to extract thickness and optical constants of a multilayer system simultaneously. Note that the complex dielectric function $\varepsilon = \varepsilon_r + i\varepsilon_i$ is the key optical parameter of a material for figuring out the electronic band structure and potential applications. Hence, SE makes it possible to investigate phase evolutions for PZT by the change of the imaginary part of ε and the electronic transitions [26, 27]. It should be emphasized that the experimental results should be more forcefully combined with first-principles calculations. According to the basic law of motion and the

interaction between atomic nucleus and electron, first-principles calculations of quantum mechanics solve the Schrödinger equation based on *ab initio* methods to acquire the wave functions [28, 29]. Accordingly, as a fundamental and significant technology of modern material computation and design, the first-principles with pseudopotentials method based on density functional theory (DFT) has had dramatic success and made considerable headway [30, 31]. Therefore, it is employed as a reproduced method to our experimental results and to explain the physical origins.

In the present work, we carried out a linked study of measured complex dielectric functions and calculated the electronic band structure of PZT based on temperature dependent SE and first-principles calculations. The main objective of our study was to explore optical constants, origins of electronic transitions and phase transitions of PZT ceramics systematically in a wide range of compositions and temperatures. At the end of the PZ, a likely Zr-rich ion cluster was presumed firstly, and the observed Zr-side intermediate (named I-m) phase is attributed to the tilting competition. Moreover, a certain border of the monoclinic region near $x = 0.28$ has been detected and the interesting phenomenon is that the rhombohedral field defined firstly by Jaffe has been shared by wide intermediate monoclinic structures [11]. Meanwhile, the origins of the two interband transitions have been clarified from the calculated band structures and complex dielectric functions. Correspondingly, we have established a relatively well-enriched phase diagram of PZT by SE and the intermediate structures can be emphatically discussed.

2. Experimental details

The ferroelectric perovskite-structure $\text{PbZr}_{1-x}\text{Ti}_x\text{O}_3$ ceramics ($x = 0.05, 0.10, 0.30, 0.40, 0.48, \text{ and } 0.70$) were fabricated by a conventional solid-state reaction sintering procedure. All the raw materials of lead tetraoxide (Pb_3O_4), zirconium dioxide (ZrO_2), titanium dioxide (TiO_2) had undergone a sintering process in a lead rich environment due to the lead volatilization. The samples were sintered at 1300 °C for 1 h in air atmosphere before being processed into wafers with the diameter of 12 mm and the thickness of 1 mm. Note that more fabrication details can be found elsewhere [32, 33]. Furthermore, all the PZT ceramics were single-side polished, then cleaned in pure ethanol with an ultrasonic bath and rinsed by deionized water successively before the spectral measurements.

To study the complex dielectric functions and interband electronic transitions of the PZT ceramics, temperature dependent SE experiments were implemented using the vertical variable angle near-infrared-ultraviolet SE (V-VASE by J.A. Woollam Co., Inc.) in the photon energy range of 2.0–6.0 eV. The ellipsometric angles Ψ and Δ were collected at each 5 nm with a settled incident angle of 70° and the high accuracy measurements were ensured with the aid of an auto retarder. To fulfill a temperature variation from 4 to 800 K with a precision of about ± 1 K, the PZT ceramics were fixed into Janis CRV-275V with liquid helium and Instec cell with liquid nitrogen as well as water pump cooling accessories for the low and high temperature region, respectively. The ellipsometric

spectra were analyzed with the WVASE32 software package. Note that the window effect was eliminated by calibrating the silicon sample.

First-principles theory calculations have been performed successfully in inquiring into the piezoelectric and ferroelectric perovskite materials. In this work, we carried out the plane-wave pseudopotential calculations based on DFT to elucidate the origins of the interband transition critical point (CP) features, at the level of the generalized gradient approximation (GGA) with the Perdew–Burke–Ernzerhof (PBE) functions. The cutoff kinetic-energy is 680 eV for the cubic perovskite structures PZ and PT. We employed a $6 \times 6 \times 6$ Monkhorst–Pack k -point mesh for the Brillouin-zone integration after taking the convergence tests with 10^{-6} eV as the criterion energy. The Hellmann–Feynman force of each atom was set to be less than 0.01 eV \AA^{-1} and the tolerances were $5 \times 10^{-6} \text{ eV atom}^{-1}$ considering the converged structures. We conducted the electronic structure calculations with the optimized lattice geometries using the Materials Studio 7.0 Package. The calculated complex dielectric functions ϵ can be obtained based on optical analysis and the Kramers–Kronig relation.

3. Results and discussion

SE as a powerful technique has several special advantages. Firstly, the surface roughness effect can be better minimized and the sensitivities to both the defects and instabilities of the light source are relatively tiny [34]. Moreover, the polarized light of SE is extremely suitable to study anisotropic materials as to the various orientation of the electric field vector to the optical axes. In addition, based on Kramers–Kronig-consistency, the real and imaginary parts of ϵ in a wide photon energy range can be accurately determined. Optical properties of the PZT ceramics were obtained by temperature dependent SE. It should be noted that the complex ratio $\rho = R_p/R_s = \tan \Psi e^{i\Delta}$, [35] in which R_p and R_s are the complex reflection coefficient of the parallel and perpendicular directions of the polarized incident light, respectively. Then in consideration of the surface roughness, the relation to the pseudodielectric functions is conducted by $\langle \epsilon \rangle = \langle \epsilon_r \rangle + i \langle \epsilon_i \rangle = \sin^2 \theta + [(1 - \rho)/(1 + \rho)]^2 \tan^2 \theta \sin^2 \theta$, here θ is the incident angle [36]. We modeled a three-layer structure (air/surface rough layer/PZT ceramic) to fit the pseudodielectric functions. Particularly, the surface rough layer was considered presumably as a mixture of 50% PZT bulk material and 50% void constituent according to the Bruggeman effective medium approximation (EMA). Because the grain size of about 42 nm is relatively tiny compared with the incident light spot of about 1 mm, the scattering effects were not taken into account [37].

Figures 1(a)–(c) display the derived real ϵ_r and imaginary ϵ_i parts of the complex dielectric functions for partial PZT ceramics ($x = 0.05, 0.30$, and 0.70) in the spectral range of 2.0–6.0 eV at several temperatures of 4, 300, and 500 K, respectively. In the fitting process, we employed two parametric oscillators to evaluate the dielectric functions involving

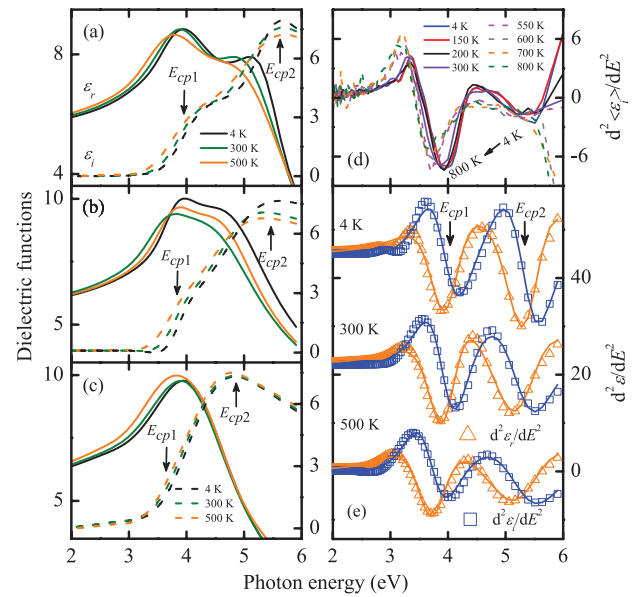


Figure 1. Real (solid lines) and imaginary (dashed lines) parts of the complex dielectric functions for PZT ceramics measured at 4, 300 and 500 K for (a) $x = 0.05$, (b) $x = 0.30$ and (c) $x = 0.70$. (d) The second partial derivative spectra for the imaginary part of the pseudodielectric function for PZT ceramics ($x = 0.05$) at various temperatures. (e) The second derivatives of the complex dielectric functions spectra (symbols) and the best-fitted (solid lines) at 4 K (+40 in absolute value of ϵ), 300 K (+20 in absolute value of ϵ) and 500 K for PZT ceramic ($x = 0.05$). Two interband transition E_{cp1} and E_{cp2} features are marked by arrows.

Psemi-M0 and Psemi-M3 [38, 39]. Accordingly, the thickness of the roughness layer was fitted to be about 8.4 nm, which is identified well with the results of the surface morphology by atomic force microscopy (AFM). All of the well-fitted dielectric spectra exhibit obvious evolutions with the variation compositions of Ti as well as the temperature. It is remarkable that the imaginary part ϵ_i of all PZT ceramics is in close proximity to zero below the absorption edge, indicating that no possible states have been detected within the band gap introduced by surface or bulk defects [40]. With further increasing photon energy, ϵ_i shows a sudden aggrandizement derived from a strong absorption (near about 3.5 eV). Above the absorption edge, all the ϵ spectra are dominated by two intense interband excitonic absorption CP features around 3.8 eV and 5.0 eV, marked by arrows in figures 1(a)–(c) (hereinafter, E_{cp1} and E_{cp2}). At the Zr-rich side of the PZT ceramics as $x = 0.05$, two noticeable interband transitions are captured more lightly, as compared with that in PZT with $x = 0.70$. Along with the enhance ratio of Ti, E_{cp2} decreases gradually, which is attributed to the difference of the metallic state energies between Ti 3d and Zr 4d. On the other hand, E_{cp1} is not as sensitive to the alternative components as E_{cp2} for the reason that the energies of the related electronic states remain nearly constant [41, 42]. It is obvious that the CP features at low temperatures such as 4 K are better determined than those at higher temperatures. In addition, a red shift phenomenon occurs with the elevated temperature for both E_{cp1} and E_{cp2} in each component, which can be mainly ascribed to the well-known temperature effects derived from the lattice thermal

Table 1. Parameters of the SCP model for PZT ($x = 0.05, 0.30, 0.48, \text{ and } 0.70$) ceramics extracted from the best fitting second derivatives of the complex dielectric functions at several temperatures.

Samples Temperature (K)	$x = 0.05$			$x = 0.30$			$x = 0.48$			$x = 0.70$		
	4	300	500	4	300	500	4	300	500	4	300	500
A_1	1.89 (0.06)	1.67 (0.06)	1.44 (0.10)	0.84 (0.08)	0.76 (0.04)	0.76 (0.01)	0.56 (0.04)	0.57 (0.06)	0.60 (0.01)	3.13 (0.44)	2.33 (0.10)	2.07 (0.06)
ϕ_1 (deg)	20.54 (0.11)	20.88 (0.13)	20.42 (0.09)	19.88 (0.07)	20.09 (0.08)	20.03 (0.04)	20.17 (0.17)	20.17 (0.06)	9.94 (0.08)	19.93 (0.08)	19.96 (0.05)	19.92 (0.05)
E_{cp1} (eV)	3.95 (0.02)	3.95 (0.03)	3.71 (0.02)	3.79 (0.01)	3.73 (0.01)	3.59 (0.01)	3.79 (0.03)	3.70 (0.02)	3.54 (0.02)	3.99 (0.01)	3.90 (0.01)	3.72 (0.01)
Γ_1 (eV)	0.66 (0.01)	0.62 (0.01)	0.66 (0.02)	0.45 (0.02)	0.46 (0.02)	0.52 (0.01)	0.41 (0.01)	0.44 (0.02)	0.50 (0.01)	0.83 (0.03)	0.78 (0.01)	0.79 (0.01)
A_2	3.28 (0.36)	4.75 (0.39)	5.15 (0.87)	5.70 (0.91)	5.86 (0.92)	5.98 (0.09)	5.73 (0.48)	5.33 (0.25)	6.08 (0.17)	7.34 (0.65)	8.25 (0.34)	7.62 (0.13)
ϕ_2 (deg)	14.70 (0.07)	14.80 (0.06)	14.95 (0.13)	15.02 (0.07)	15.10 (0.16)	14.90 (0.03)	14.93 (0.07)	14.83 (0.01)	14.86 (0.02)	15.39 (0.07)	15.21 (0.03)	15.32 (0.02)
E_{cp2} (eV)	5.38 (0.01)	5.28 (0.03)	5.33 (0.06)	5.06 (0.03)	4.93 (0.06)	4.75 (0.02)	4.72 (0.03)	4.63 (0.01)	4.54 (0.01)	4.58 (0.02)	4.56 (0.02)	4.63 (0.01)
Γ_2 (eV)	0.73 (0.04)	0.94 (0.01)	1.12 (0.07)	1.13 (0.07)	1.11 (0.06)	1.24 (0.01)	1.02 (0.04)	0.99 (0.02)	1.08 (0.01)	1.35 (0.06)	1.39 (0.01)	1.28 (0.01)

Note: Note that the 95% confidence limit of the fitting parameters is given in parentheses.

expansion and the band structure renormalization induced by electron–phonon interaction [43, 44].

It is well known that the complex dielectric function ε , which shows a characteristic peak or shoulder structures, is closely associated with the electronic transitions. The relationships among them are connected by the standard critical point (SCP) model, $\varepsilon = C - Ae^{i\phi}(E - E_g + i\Gamma)^n$, [44] where A is the amplitude, E_g is the threshold energy, Γ is the broadening parameter, and ϕ is the excitonic phase angle. Furthermore, the exponent n values of $-1, -1/2, 0$, and $1/2$ denote excitonic, one-, two- and three-dimensional line shapes, respectively. It is valid and accurate to calculate the derivative of the complex dielectric functions for ascertaining the transition energies. Choi *et al* have investigated the accurate CP energies of cubic FeS₂ by fitting standard line shapes to second energy derivatives of the $\langle \varepsilon \rangle$ data and analyzed the origins of the six CP features combined with DFT calculations [23]. Specifically, the obtained electronic transitions by the derivative of complex dielectric functions are independent of the surface roughness layer. To determine the electronic transitions and paraelectric (PE) to ferroelectric phase transformation, we calculated the second partial derivative spectra for the imaginary part of the pseudodielectric function $\langle \varepsilon_i \rangle$ at different temperatures, as illustrated in figure 1(d) for PZT with $x = 0.05$ as an example. Two evident dips dominate the derivative spectra, which indicates that there are two probed transitions at temperatures below 500 K. While at higher temperature, there remains a noticeable drop, and another transition cannot be detected. This abnormal phenomenon can be explained by the fact that a PE–FE phase transformation arises at about 500 K in the Zr-rich domains.

Correspondingly, the accurate energies of CP features have been obtained for further studies of phase transformation through fitting the second derivative of the complex dielectric

functions. Note that the expression of the second derivative can be written as the following:

$$\frac{d^2\varepsilon}{dE^2} = \begin{cases} n(n-1)A_m e^{i\phi_m}(E - E_m + i\Gamma_m)^{n-2}, & n \neq 0 \\ A_m e^{i\phi_m}(E - E_m + i\Gamma_m)^{-2}, & n = 0, \end{cases} \quad (1)$$

where the real and imaginary parts were fitted synchronously and parameter m represents the total number of oscillators used in the fitting process. For the $d^2\varepsilon/dE^2$ spectra in figure 1(e), all CP features are resolved primarily with the minimized experimental noise. Obviously, two evident transitions are observed, which elucidate that the second derivative employed in the present work can separate the weak transition features successfully. Each transition labeled in figure 1(e) shows a red shift trend along with increasing the temperature. In addition, the CP peaks have exhibited a broadening trend due to the temperature effects. For example, table 1 displays the fitting parameters at three temperatures for comparison.

It is crucial to detect and figure out the mechanisms of phase transformations for theoretical design and practical development of novel function materials. For more detailed phase transitions of PZT, we focus on the temperature evolution of the interband transitions from 4 K to 500 K. As shown in figure 2, each set of CP features can be divided into three parts with different phases according to temperature dependence of E_{cp2} energy. Note that E_{cp1} has a similar variation trend and is dominated by A-cation p orbitals and O-anion p orbitals. While E_{cp2} is associated tightly with B-cation d orbitals and presents a more sensitive relationship to the composition variation. By referring to the reported studies, each partitioned phase region and corresponding space groups are determined [11, 15, 19]. Fortunately, an AFE_o region was detected merely at the Zr-rich side with the space group of $Pbam$. On the other hand, the [FE_{R(HT)}] ones appear at high temperature of each set. It is worth mentioning that the thermal broadening of optical

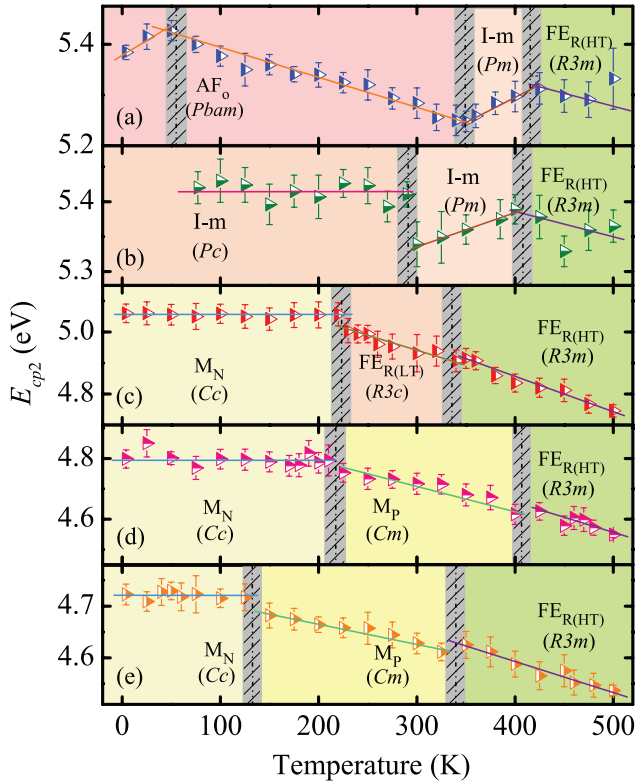


Figure 2. (a)–(e) The thermal evolution of E_{cp2} energy for PZT ceramics ($x = 0.05, 0.10, 0.30, 0.40,$ and $0.48,$ respectively). The shaded stripes show the boundaries of adjacent phases. Note that all CP energies are linearly fitted with the solid lines to guide the eyes.

transitions may be reduced, such as the features of $[FE_{R(HT)}]$ ones [45]. In fact, these tiny changes of $[FE_{R(HT)}]$ structure can be used to verify the previous studies of phase diagrams, instead of intending to specify the location of the phase boundaries. For $x = 0.05$ in figure 2(a), a mysterious I-m phase with space group Pm and a width of 50 K separates the AFE_0 and $[FE_{R(HT)}]$ at about 350 K. Interestingly, a drop of E_{cp2} emerges at temperatures below 70 K, which is located near the boundary of AFE_0 and I-m structures. This abnormal behavior is attributed to the Zr-rich ion clusters. For $x = 0.10$, an $a^-b^-b^-$ tilted cell with Pc symmetry was discovered unequivocally to distinguish from Pm at 300 K, which has always been undiscovered due to the narrow field. While increasing Ti compositions to about 0.30, there is a monoclinic region M_N with Cc features in the temperature region just below the $[FE_{R(LT)}]$ phase. As for $x = 0.40$ and $x = 0.48$, the interband transitions can be divided into M_N , M_P and $[FE_{R(HT)}]$. Note that the intermediate monoclinic phase near the MPB is composed of M_N and M_P . It signifies positive when the direction of Pb displacements rotates towards $[0\ 0\ 1]_p$ as M_P , while negative means rotating towards $[1\ 1\ 0]_p$ as M_N . Overall, each set of transition energies displays a similar red shift trend following the temperature. Other than partial intermediate structures, the temperature coefficients are typical with a magnitude of about 10^{-4} eV K^{-1} . The abnormal phenomena may be attributed to the complex micro-domain structures close to intermediate regions [15, 19].

Relative to the half empirical method, first-principles calculations merely employ several basic physical quantities

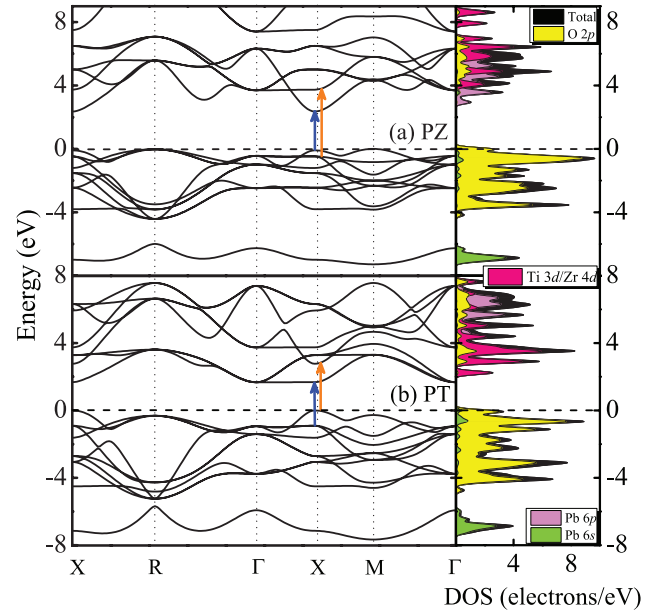


Figure 3. Calculated band structure and corresponding density of states for (a) PZ and (b) PT. Note that the related transitions are indicated by arrows.

such as the mass of electron and the speed of light to predict the properties of micro systems. At present, the energy band theory has been widely used to explain and forecast the fundamental characters of solids. Experimental spectra can be interpreted qualitatively by the main features of band gap, density of states, and the width of valence bands. Furthermore, optical properties produced by electronic transitions can be obtained via theoretical calculations. In regard to the origins of the detected transitions, we combined both the previous and present computational conclusions with our experimental results to propose the evolution of the interband transitions [46, 47]. The calculated band structure, partial and total density of states (DOS) for $PbZrO_3$ (PZ) and $PbTiO_3$ (PT) in cubic structure are displayed in figures 3(a) and (b). The tops of the valence band contain mixed O $2p$ and Pb $6s$ states and the lower valence ones are mostly pure O $2p$ for both PZ and PT. While from the DOS, the bottoms of conduction band are dominated by Pb $6p$ -like states at low Ti composition and then convert into metal d states with more Zr content substituted by Ti. Similarly, the higher conduction bands in the range of 3–4 eV originate from Zr $4d$ and Pb $6p$ states for PZ and PT, respectively. This unique fact can be interpreted by the coupling between metal d states and Pb $6p$ -like states derived from intrinsic alloy disorder along with the accessory Ti content [41].

As shown in figures 4(a) and (b), the calculated dielectric functions manifest two strong absorptions with a well-known problem of the underestimated optical energies of transitions by about 0.20–0.30 [23, 47]. The dominant CP features observed experimentally are captured by the DFT calculations, and the corresponding second derivative of the complex dielectric functions spectra are displayed in figures 4(c) and (d) for PZ and PT, respectively. The calculated results are also consistent with the experimental ones except for the higher

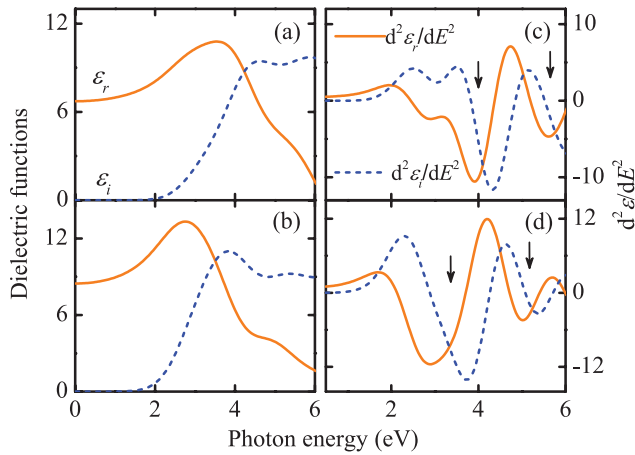


Figure 4. Theoretical dielectric functions for (a) PZ and (b) PT. The corresponding second derivatives of the dielectric functions for (c) PZ and (d) PT. The transitions features are marked by arrows.

CP energies, which cannot be detected by SE measurements. Therefore, based on theoretical calculations and SE experiments, we can conclude that E_{cp1} is assigned to the transitions of $O\ 2p/Pb\ 6s \rightarrow Pb\ 6p$, and E_{cp2} is mostly attributed to both transitions of $O\ 2p \rightarrow Pb\ 6p$ and $O\ 2p \rightarrow Zr\ 4d$ for PZ as well as low Ti compositions. In contrast, for PZT with abundant Ti components, we proffer that the transitions of $O\ 2p \rightarrow Ti\ 3d$, and mixed $O\ 2p/Pb\ 6s \rightarrow Pb\ 6p$ with $O\ 2p \rightarrow Pb\ 6p$ are devoted to E_{cp1} and E_{cp2} , respectively. The origins of the interband transitions have been assigned according to our computational band structures and anterior experimental results [41, 47].

However, the E_{cp1} captured by SE measurement for PZT with various Ti compositions are actually the lower energy transitions instead of occurring at appointed locations. Therefore, the assignment of origins could suggest certain differences from the reported ones due to the band crossing of metal d states and Pb p states. Note that the complicated physical origins of the interband transitions in PZT probably originate from the coupling of Zr/Ti d states and Pb $6p$ -like states, as well as the alloy disorder. Besides, one would find that the calculated results cohere exactly with those from SE experimental results included in figure 1. The result indicates that the present first-principles calculations are reliable and can be used to make qualitative analysis combined with experimental results.

Figure 5 displays the phase diagram for PZT. It is dominated by PE–FE and AFE_O – FE_R – FE_T phase transitions as functions of temperatures and Ti concentrations. Two intermediate phases were detected explicitly among AFE, FE_R and FE_T regions. For ferroelectric phase transformation materials, a phase boundary is considered as ion clusters with different size or charge proved by TEM images and other physical evidence [22, 48]. It is worth raising that the lines were obtained by the phase transition temperatures extracted from figure 2, meanwhile based on the previous studies of the phase diagram. In addition, the phase boundaries in the phase diagram for PZT are intended to illuminate two significant intermediate phases, instead of specifying precise compositions or

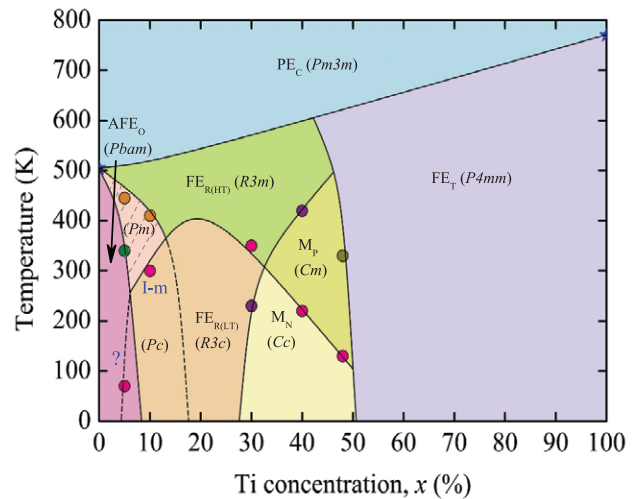


Figure 5. The phase diagram of PZT ceramics derived from the thermal evolution of the transition energies with the temperature and Ti compositions. The phase transformation temperatures extracted from figure 2 in this work are marked with the solid circle dots and the star symbols with the compositions of $PbZrO_3$ and $PbTiO_3$ are from [11]. Note that the likely Zr-rich iron clusters at the end of $PbZrO_3$ are marked with a question mark and are in need of further studies.

phase transition temperatures. As shown in figure 5, around $x = 0.08$, the I-m phase emerges when the transition is frustrated by the near matrix, probably Zr-rich ion clusters here, which is marked by the question mark and in need of further studies. That is to say, the switch of Pb^{2+} displacements from along with $[1\ 1\ 0]_p$ directions in AFE phase to $[1\ 1\ 1]_p$ in FE_R phase is discomfited by the impact of the ion clusters. In the AFE_O region, we can see a special field with a dashed line, which has not been mentioned before. Considering that it is located near the AFE–FE boundary and contains a small drop of the transition energies in figure 2, one may deduce that the Zr-rich ion clusters is present at about 70 K. The I-m phase extends approximately from $x = 0.08$ to 0.16, which can be divided into the space group Pm and Pc . The Pc cell with the $a^-b^-b^-$ system allows the coupling of both tilt and Pb^{2+} displacements, in contrast, the Pm ones with the $a^0a^0a^0$ system merely permits the displacements of Pb^{2+} . Therefore, a tilt transition temperature border in the I-m regions is introduced, which connects the drop border of the FE_R structure. The difference of the tilt between the $R3m$ and $R3c$ structures makes shorter coherence lengths and accordingly leads to a remarkable drop of the onset temperature for the tilt transitions. It is understandable that we attribute the border at $x = 0.16$ of the intermediate to a tilting competition between the $[FE_{R(HT)}]$ and $[FE_{R(LT)}]$. Also the reported study has proposed that it is the onset of tilt instability and the cation disorder that likely hinder the formation of tilt patterns with long-range order well [15].

It is generally known that ferroelectricity is associated with the atomic offcenter displacements, which depends on a subtle balance between long-range Coulomb interaction and short-range covalent interaction [49]. Phase transitions of the ferroelectric materials would be reasonably related to the

polarization. At the composition close to MPB, the rotations of polarization become continuous in a intermediate monoclinic phase from $[1\ 1\ 1]_p$ toward $[0\ 0\ 1]_p$ directions severally in R and T domains, which maximize the performance of PZT. The M phase has been accepted and given a wide range with an uncertain boundary based on the reported work [16, 19, 50]. According to the cluster model, we can deduce that a cluster including similar Pb^{2+} displacements would occur as approaching the MPB region. Then the transformation from R to M structure is characterized by a certain size or charge of clusters. Compared to the present data, we have proffered the border between R and M regions at about $x = 0.30$. In figure 5, there are two certain fields located at the MPB domains, which have already been defined as M_p and M_n relying on the rotation directions of the displacements. Actually, the space group Cc is distinguished from Cm just by the directions of the cation displacements. The border between them is a stretching from the R field. Although Cc is the subgroup of both Cm and $R3m$, the hypothesis about the coexistence of Cm and Cc at low temperatures may prove to be invalid. It is well-coincident with our phase diagram that the Cm phase dose not persist below 200 K [20]. Consequently, with the further movement of the polarization to $[0\ 0\ 1]_p$, a M–T phase transition appears. The discoveries of Zr-rich ion clusters and two intermediate phases have clarified that the evolutions of electronic transitions can be directly applied to estimate the phase transformations in ferroelectric materials.

4. Summary

In conclusion, optical properties and interband electronic transitions of PZT ceramics as functions of temperatures and Ti concentration have been investigated by temperature dependent SE. The intrinsic characteristics of the phase transformations and phase diagram for PZT are derived. Fortunately, we proposed remarkable Zr-rich ion clusters at low temperature and the I-m phase near the PZ end is captured at about $x = 0.08$ to 0.16 as a result of the tilting competitions of the $[\text{FE}_{\text{R(HT)}}]$ and $[\text{FE}_{\text{R(LT)}}]$. The intermediate M region owns a more wide compositions range approximately from $x = 0.28$ to 0.50. Note that a larger M domain makes it possible to adjust a more superior performance through external strains, electric field or magnetic field near the MPB for PZT. We have made density functional calculations to reproduce our experimental results and explore the origins of the relative interband transitions. Eventually, the establishment of an optimized phase diagram for PZT sheds light on the significant roles of the SE method together with first-principles calculations in ferroelectric oxides.

Acknowledgments

One of the authors (M J Li) is grateful to Dr Z H Duan, Dr K Jiang, X J Ding, Q L Deng and P Zhang for technical support. This work was financially supported by Major States Basic Research Development Program of China (Grant Nos. 2011 CB922200 and 2013CB922300), the Natural Science

Foundation of China (Grant Nos. 11374097, and 61376129), Projects of Science and Technology Commission of Shanghai Municipality (Grant Nos. 15JC1401600, 14XD1401500, 13JC1402100, and 13JC1404200), and the Program for Professor of Special Appointment (Eastern Scholar) at Shanghai Institutions of Higher Learning.

References

- [1] Scott J F and Paz De Araujo C A 1989 *Science* **246** 1400
- [2] Yang X L, Su X D, Shen M R, Zheng F G, Xin Y, Zhang L, Hua M C, Chen Y J and Harris V G 2012 *Adv. Mater.* **24** 1202
- [3] Baghaie Yazdi M, Choi K Y, Wulferding D, Lemmens P and Alff L 2013 *New J. Phys.* **15** 103032
- [4] Dawber M, Rabe K M and Scott J F 2005 *Rev. Mod. Phys.* **77** 1083
- [5] Dass M L A, Dahmen U, Thomas G, Yamamoto T and Okazaki K 1986 *IEEE Trans. Ultrason. Ferroelectr. Freq. Control* **33** 801
- [6] Jin Y M, Wang Y, Khachatryan A G, Li J F and Viehland D 2003 *Phys. Rev. Lett.* **91** 197601
- [7] Agar J C et al 2014 *Adv. Mater. Interfaces* **1** 1400098
- [8] Theissmann R, Schmitt L A, Kling J, Schierholz R, Schonau K A, Fuess H, Knapp M, Kungl H and Hoffmann M J 2007 *J. Appl. Phys.* **102** 024111
- [9] Gaponenko I, Tückmantel P, Karthik J, Martin L W and Paruch P 2015 *Appl. Phys. Lett.* **106** 162902
- [10] Wang Y U 2007 *Phys. Rev. B* **76** 024108
- [11] Jaffe B, Cook W R and Jaffe H 1971 *Piezoelectric Ceramics* (London: Academic)
- [12] Fu H and Cohen R E 2000 *Nature* **403** 281
- [13] Damjanovic D and Demartin M 1997 *J. Phys.: Condens. Matter* **9** 4943
- [14] Mangalam R V K, Agar J C, Damodaran A R, Karthik J and Martin L W 2013 *ACS Appl. Mater. Interfaces* **5** 13235
- [15] Cordero F, Trequattrini F, Craciun F and Galassi C 2013 *Phys. Rev. B* **87** 094108
- [16] Noheda B, Cox D E, Shirane G, Gonzalo J A, Cross L E and Park S-E 1999 *Appl. Phys. Lett.* **74** 2059
- [17] Catalan G, Lubk A, Vlooswijk A H G, Snoeck E, Magen C, Janssens A, Rispens G, Rijnders G, Blank D H A and Noheda B 2011 *Nat. Mater.* **10** 963
- [18] Pandey D, Singh A K and Baik S 2008 *Acta Crystallogr. A* **64** 192 (SGCAPL2012)
- [19] Zhang N, Yokota H, Glazer A M, Ren Z, Keen D A, Keeble D S, Thomas P A and Ye Z-G 2014 *Nat. Commun.* **5** 5231
- [20] Woodward D I, Knudsen J and Reaney I M 2005 *Phys. Rev. B* **72** 104110
- [21] Narayanan M, Tong S, Liu S, Ma B and Balachandran U 2013 *Appl. Phys. Lett.* **102** 062906
- [22] Knudsen J, Woodward D I and Reaney I M 2003 *J. Mater. Res.* **18** 262
- [23] Choi S G, Hu J, Abdallah L S, Limpinsel M, Zhang Y N, Zollner S, Wu R Q and Law M 2012 *Phys. Rev. B* **86** 115207
- [24] Zhang X L, Hu Z G, Xu G S, Zhu J J, Li Y W, Zhu Z Q and Chu J H 2013 *Appl. Phys. Lett.* **103** 051902
- [25] Zhang J Z et al 2015 *Phys. Rev. B* **91** 085201
- [26] Tyunina M, Dejneka A, Chvostova D, Levoska J, Plekh M and Jastrabik L 2012 *Phys. Rev. B* **86** 224105
- [27] Dejneka A, Aulika I, Trepakov V, Krepelka J, Jastrabik L, Hubicka Z and Lynnyk A 2009 *Opt. Express* **17** 14322
- [28] Vanderbilt D 1990 *Phys. Rev. B* **41** 7892
- [29] Ponomareva I, Tagantsev A and Bellaiche L 2012 *Phys. Rev. B* **85** 104101

- [30] Kornev I A, Bellaiche L, Janolin P-E, Dkhil B and Suard E 2006 *Phys. Rev. Lett.* **97** 157601
- [31] Hong J and Vanderbilt D 2013 *Phys. Rev. B* **88** 174107
- [32] Chen X F, Dong X L, Zhang H L, Feng N B, Nie H C, Cao F, Wang G S, Gu Y and He H L 2009 *J. Appl. Phys.* **105** 096104
- [33] Chen X, Jiang K, Hu Z G, Chen X F, Wang G S, Dong X L and Chu J H 2013 *Appl. Phys. Lett.* **101** 011914
- [34] Gori P, Rakel M, Cobet C, Richter W, Esser N, Hoffmann A, Sole R D, Cricenti A and Pulci O 2010 *Phys. Rev. B* **81** 125207
- [35] Park J M, Lynch D W, Lee S J, Schlagel D L, Lograsso T A, Tsokol A O, Snyder J E and Jiles D C 2006 *Phys. Rev. B* **73** 035110
- [36] Yang H H U, D'Archangel J, Sundheimer M L, Tucker E, Boreman G D and Raschke M B 2015 *Phys. Rev. B* **91** 235137
- [37] Schoenes J, Barkow U, Broschwitz M, Oppeneer P M, Kaczorowski D and Czopnik A 2000 *Phys. Rev. B* **61** 7415
- [38] Herzinger C M and Johs B D 1998 *US Patent* No. 5-796-983
- [39] Jiang P P, Duan Z H, Xu L P, Zhang X L, Li Y W, Hu Z G and Chu J H 2014 *J. Appl. Phys.* **115** 083101
- [40] Zhang Y N, Hu J, Law M and Wu R Q 2012 *Phys. Rev. B* **85** 085314
- [41] Kang T D, Lee H, Xing G, Lzumskaya N, Avrutin V, Xiao B and Morkoç H 2007 *Appl. Phys. Lett.* **91** 022918
- [42] Lee H *et al* 2005 *J. Appl. Phys.* **98** 094108
- [43] Fan H Y 1951 *Phys. Rev.* **82** 900
- [44] Ding X J, Xu L P, Hu Z G, Chen X F, Wang G S, Dong X L and Chu J H 2014 *Appl. Phys. Lett.* **105** 131909
- [45] Choi S G, Chen R, Persson C Kim T J, Hwang S Y and Kim Y D 2012 *Appl. Phys. Lett.* **101** 261903
- [46] Mangalam R V K, Karthik J, Damodaran A R, Agar J C and Martin L W 2013 *Adv. Mater.* **25** 1761
- [47] Lee H *et al* 2005 *Appl. Phys. Lett.* **86** 262902
- [48] Karthik J, Ager J C, Damodaran A R and Martin L W 2012 *Phys. Rev. Lett.* **109** 257602
- [49] Cohen R E 1992 *Nature* **358** 136
- [50] Noheda B, Wu L and Zhu Y 2002 *Phys. Rev. B* **66** 060103